

# XAMI - A Benchmark Dataset for Artefact Detection in XMM-Newton Optical Images

Elisabeta-Iulia Dima<sup>\*1</sup>, Pablo Gómez<sup>2</sup>, Sandor Kruk<sup>2</sup>, Peter Kretschmar<sup>2</sup>,  
Simon Rosen<sup>3</sup>, Călin-Adrian Popa<sup>1</sup>

<sup>1</sup>Department of Computers and Information Technology, Politehnica University of Timișoara, Blvd. V. Pârvan, No. 2, 300223 Timișoara, Romania

<sup>2</sup>European Space Agency (ESA), European Space Astronomy Centre (ESAC), Camino Bajo del Castillo s/n, 28692 Villanueva de la Cañada, Madrid, Spain

<sup>3</sup>Serco Ltd., ESAC, Camino Bajo del Castillo s/n, 28692 Villanueva de la Cañada, Madrid, Spain

Reflected or scattered light produce artefacts in astronomical observations that can negatively impact the scientific study. Hence, automated detection of these artefacts is highly beneficial, especially with the increasing amounts of data gathered. Machine learning methods are well-suited to this problem, but currently there is a lack of annotated data to train such approaches to detect artefacts in astronomical observations. In this work, we present a dataset of images from the XMM-Newton space telescope Optical Monitoring camera showing different types of artefacts. We hand-annotated a sample of 1000 images with artefacts which we use to train automated ML methods. We further demonstrate techniques tailored for accurate detection and masking of artefacts using instance segmentation. We adopt a hybrid approach, combining knowledge from both convolutional neural networks (CNNs) and transformer-based models and use their advantages in segmentation.

The presented method and dataset will advance artefact detection in astronomical observations by providing a reproducible baseline. All code and data are made available publicly<sup>1,2</sup>.

## 1 Introduction

Astronomical surveys and space missions (e.g., LSST [1] and European Space Agency’s Euclid mission [2]) will enhance our understanding of the cosmos by delivering unprecedented images, measurements and insights into billions of stars and galaxies, the expansion of the Universe, dark energy and dark matter. Such surveys will produce enormous amounts of data daily, thus the ongoing demand for the effective processing and analysis of large image data

produced by space missions underscores the necessity for automated methodologies. The presence of artefacts (e.g. *ghost* reflections, star loops, read-out streaks) (e.g., Figure 1) poses challenges, potentially leading to false detections or affecting the photometric measurements of genuine sources.

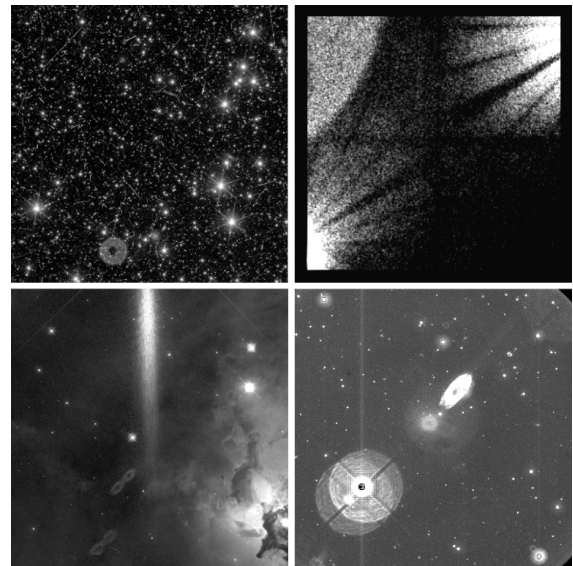


**Figure 1:** Examples of artefacts in various space missions. **(upper left)** An optical *ghost* detected in Euclid’s First Light near-infrared images. **(upper right)** *Ghost* rays and stray light patterns present in NuSTAR mission. **(bottom left)** Star loops and *dragon’s breath* artefacts appearing in the Hubble Space Telescope images. **(bottom right)** Star loops and streaks present in the XMM-Newton Optical Monitor.

**XMM-Newton Optical Monitor.** ESA’s X-ray Multi-Mirror Mission (XMM-Newton) [3, 4] is an orbiting observatory with the principal goal to conduct detailed X-ray spectroscopy of various celestial objects.

<sup>\*</sup>Corresponding author. Email: iuliaelisa15@yahoo.com

<sup>1</sup><https://github.com/ESA-DataLabs/XAMI-model>

<sup>2</sup><https://github.com/ESA-DataLabs/XAMI-dataset>

The XMM-Newton Optical Monitor (XMM-OM) [5–7] extends the simultaneous observational capability of the three main X-ray telescopes into the ultraviolet and optical bands. The XMM-OM source catalogue is a valuable resource containing approximately 9 million detections of around 6 million distinct sources. It plays a pivotal role in individual object analyses [8–10] and contributes significantly to survey science. However, the process of source detection within the XMM-OM data analysis process would benefit significantly from improved artefact recognition.

Current non-AI approaches to detecting artefacts [11–13] often struggle due to their reliance on generalised physical models. These models, while broadly applicable, fail to address specific scenarios effectively, leading to limitations in their practical utility.

AI methods based on CNN and Vision Transformer (ViT) models have achieved notable success and have benefited real-world applications in tasks such as object detection [14–17] and segmentation [18–26]. Instance segmentation techniques for astronomical sources present significant progress [27–29], yet there has been limited focus on artefacts detection [30]. ViT models are increasingly preferred in computer vision due to their self-attention mechanisms. The Segment Anything Model (SAM) [31], a ViT-based architecture, excels in class-agnostic instance segmentation and zero-shot learning, allowing it to identify objects not seen during training.

We introduce **XAMI** (*XMM-Newton optical Artefact Mapping for astronomical Instance segmentation*), a hybrid CNN and ViT-based model, and **XAMI-Dataset**, a high-precision instance segmentation dataset for astronomical images. Together, they provide a first baseline demonstrating ML-based artefact detection on astronomical images as well as benchmark and starting point for other researchers to build on.

## 2 Methods

### 2.1 Dataset

We use 1000 single-channel images at various wavelengths (see Table 1 and [32]) from the XMM-OM as the baseline artefacts dataset. Each image comprises a stack of all available windows in a given filter of an observation that, together, cover the full  $17' \times 17'$  field of view. This corresponds to a full frame of  $2048 \times 2048$  px resolution, with an effective resolution of  $0.477''/\text{pixel}$ . We rebinned the full-frame images to  $512 \times 512$  px for computational efficiency. We normalised images using *ZScaleInterval* algorithm and enhanced them with *Asinh* stretching to increase dynamic range without negatively affecting contrast.

The XAMI dataset consists of 7021 annotated artefacts which can be divided into the following categories (Figure 3):

1. *Read-Out-Streaks (ROS)* - arising from shutterless camera and continuous Charge-Coupled Device (CCD) photon recording during readout.
2. *Smoke rings (SR)* - resulting from internal reflections of starlight within the detector.
3. *Central ring (CR)* - appearing in the centre of the detector, approximately  $2'$  in diameter, resulting from background light scattering from a chamfer on the detector window mounting ring.
4. *Star loops (SL)* - elongated scattered light features caused by light from bright stars within a  $12' - 15'$  off-axis range, scattered from the chamfer.
5. *Other* - other types of artefacts which usually represent scattered light spread over large areas.

Filter	$\lambda(\text{nm})$	width	#images	#masks
V	543	70	102	880
B	450	105	116	1259
U	344	84	193	1837
UVW1(L)	291	83	403	2127
UVM2(M)	231	48	175	681
UVW2(S)	212	50	63	226
White(W)	406	347	3	11

**Table 1:** Dataset information per observing filter, together with their central wavelength and width (nm).

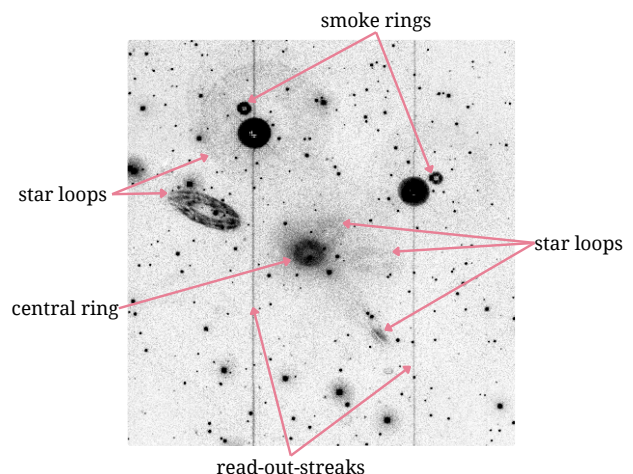


**Figure 2:** Artefacts appearing in the XMM-OM observation S0148740701 of the QSO 1939+7000 field (U filter).

We use the stratified k-fold technique to maintain consistent class proportions across dataset splits, thus

Class	Train	Validation
CR	500 (9.43%)	168 (9.75%)
SR	1267 (23.91%)	402 (23.33%)
SL	1377 (25.99%)	467 (27.10%)
ROS	2122 (40.05%)	677 (39.29%)
Other	32 (0.60%)	9 (0.52%)

**Table 2:** Dataset distribution across splits, given class labels.

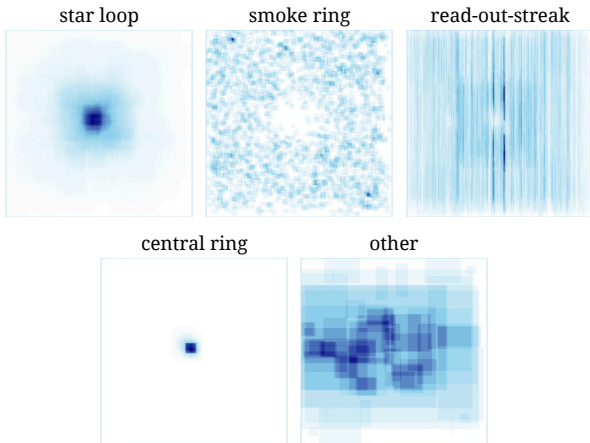


**Figure 3:** Distribution of annotation bounding boxes across different classes in the XAMI dataset.

ensuring accurate performance estimation. Resulting class distributions can be seen in Table 2.

## 2.2 Baseline Model

We propose a class-aware approach for instance segmentation that integrates an object detector, specifically the YOLOv8 model [33], into our SAM prediction logic to facilitate auto-generated input prompts.

Unlike CNNs, which strictly delineate object masks by bounding boxes, transformer-based models like SAM integrate self-attention to potentially extend beyond these initial margins. However, spatial invariance and accurate segmentation of faint objects remain a challenge for ViTs, in contrast with CNN approaches. By utilising SAM for smooth masks and YOLOv8 for faint objects with certain classes, we aim to overcome these limitations.

## 3 Results

Our methodology initially involves training SAM with ground-truth annotations using a distilled image encoder from MobileSAM [34]. For SAM, images are resized to  $1024 \times 1024$  px and have their colours normalized. We use a batch size of 8, a warmup learning rate scheduler ( $lr_{init} = 3 \times 10^{-4}$ ,  $lr_{final} = 6 \times 10^{-5}$ ) for

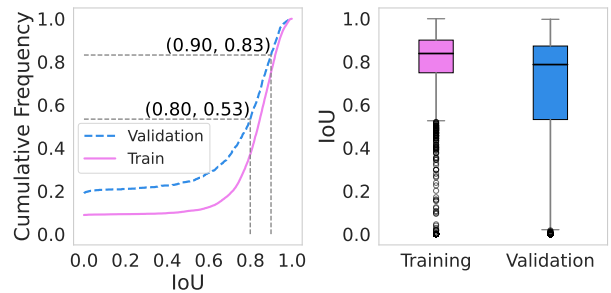


**Figure 4:** (left) Cumulative distribution of IoUs between predicted and true masks on training and validation sets. (right) Comparison of IoU distributions with higher median and consistency in training data and greater variability in validation data.

16 steps, weight decay of  $10^{-5}$  and AdamW optimizer. We train the Mask Decoder only, while freezing the Image Encoder and Prompt Embedding layers.

Following recommendations in [31], we utilise the focal loss and dice loss in a 20:1 weighted scheme. At this stage, predicted and actual masks can be directly compared. Unlike usual SAM implementations, we choose to train the Intersection-over-Union (IoU) head to provide more representative segmentation metrics. Also, when generating masks, we configure the model to allow three predicted mask outputs and select the final mask based on the highest IoU score. The total loss integrates both segmentation and IoU loss.

After training the YOLO and SAM models separately to optimise their individual performances, we freeze the YOLO layers, couple its predicted bounding boxes to the SAM Prompt Encoder and continue training the SAM Mask Decoder to refine the segmentation process for 10 additional epochs. The alignment of predicted and ground truth masks is managed using the Kuhn-Munkres assignment algorithm [35] by minimizing the IoU cost matrix. Due to higher spatial complexity of certain classes, particularly SL and *Other*, we select YOLO masks for *faint* objects of such classes at  $1\sigma$  background level, as these predictions are more stable for low-intensity artefacts. We provide the precision and recall metrics (see Table 3) using a fixed seed for reproducibility. The formulas for precision and recall are defined as follows:

$$P = \frac{TP}{TP + FP} \quad \text{and} \quad R = \frac{TP}{TP + FN} \quad (1)$$

where TP - True Positive, FP - False Positive and FN - False Negative predictions.



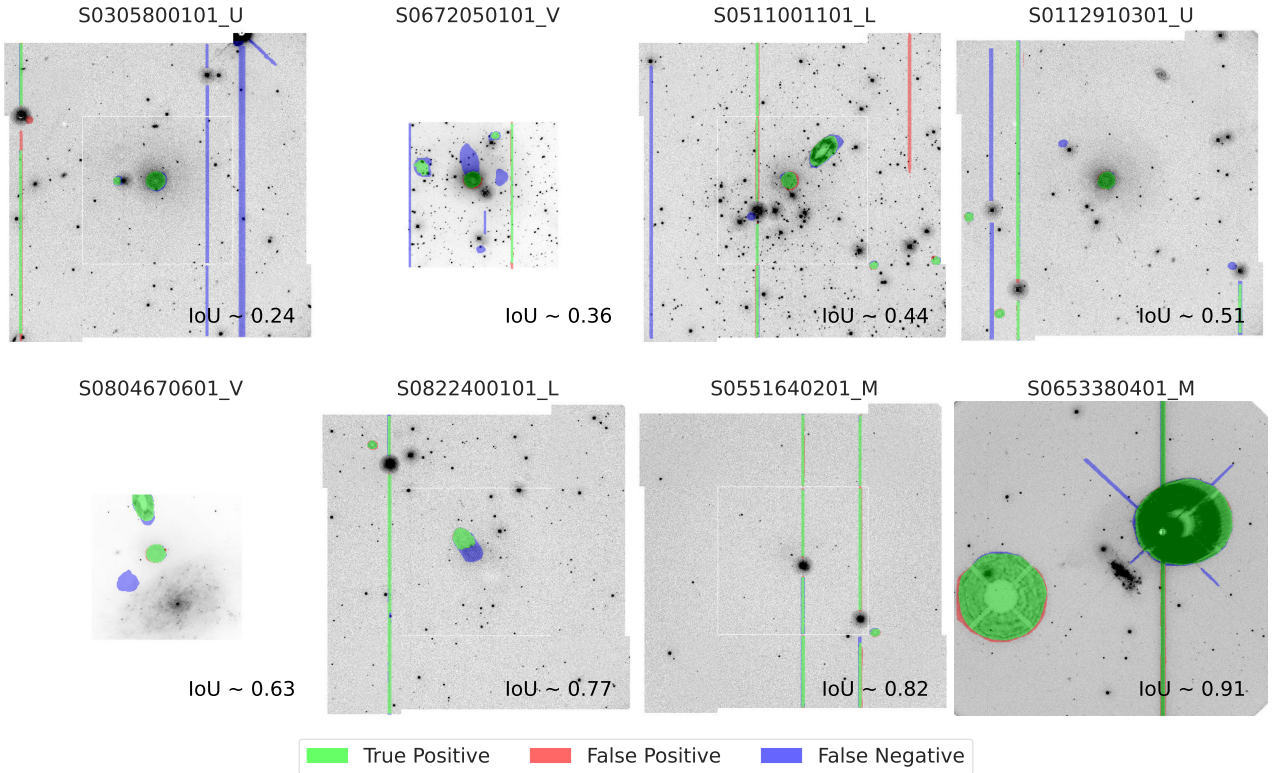


**Figure 5:** Detected masks across eight fields within the validation set, with increasing mean IoU between predicted and ground-truth masks. The mean IoU on the validation set images is  $0.658 \pm 0.207$ .

Category	Precision	Recall
Overall	84.3	72.1
CR	89.3	94.0
SR	80.6	85.6
SL	80.5	74.1
ROS	71.1	73.3
Other	100.0	33.3

**Table 3:** Precision and recall resulted from model predictions on validation set. While smaller recall for *Other* class may be caused by its under-representation, the CR class shows best overall performance, which may be attributed to its predictable location.

## 4 Discussion

In our study, we enhanced artefact detection and segmentation in XMM-Newton images by integrating CNNs with ViT-based models, significantly boosting accuracy and reducing false positives in astronomical analysis. We combined traditional YOLO models for bounding box predictions with advanced SAM models for zero-shot segmentation, demonstrating the benefits of diverse neural network strategies in ad-

ressing complex image processing challenges. Despite improvements, high variation in exposure times and intensity levels in space imagery necessitate further model refinement tailored for astronomical missions. Additionally, these variations pose challenges in dataset annotation, eventually making it difficult to establish clear thresholds for distinguishing artefacts from the background. The XAMI average end-to-end inference time per image containing annotations is 100ms, suitable for medium to large image data (up until hundreds of thousands of images similar to ours) and applications which do not particularly require instant real-time processing. The SAM heavy architecture still represents a bottleneck for prediction, with 70–80ms/image. We plan to expand our dataset with additional observations from various space missions to enhance model performance. Our goal is to benchmark our methods against other techniques in artefact detection and segmentation, while allowing the flexibility to choose or replace detectors and segmentors with novel state-of-the-art models. We will explore practical applications, such as faster data processing for space missions, and integrate our implementations into existing astronomical data processing systems. Feedback from astronomers will be crucial in further refining our approach.

**Acknowledgements.** The authors acknowledge the contribution of Inès Perez, Léa Zuili, Simon Astarita to dataset annotations. This publication uses data generated via the Roboflow.com<sup>3</sup> and Zooniverse.org<sup>4</sup> platforms.

## References

1. Ivezić, Ž. *et al.* LSST: From Science Drivers to Reference Design and Anticipated Data Products. *The Astrophysical Journal* **873**, 111. issn: 1538-4357. <http://dx.doi.org/10.3847/1538-4357/ab042c> (Mar. 2019).
2. Laureijs, R. *Euclid Assessment Study Report for the ESA Cosmic Visions* 2009. arXiv: 0912.0914 [astro-ph.CO].
3. Jansen, F. *et al.* XMM-Newton observatory. I. The spacecraft and operations. *Astronomy and Astrophysics* **365**, L1–L6 (Dec. 2000).
4. Schartel, N. *et al.* in *Handbook of X-ray and Gamma-ray Astrophysics* 1–38 (Springer Nature Singapore, 2022). isbn: 9789811645440. [http://dx.doi.org/10.1007/978-981-16-4544-0\\_41-1](http://dx.doi.org/10.1007/978-981-16-4544-0_41-1).
5. Mason, K. O. *et al.* The XMM-Newton optical/UV monitor telescope. *Astronomy and Astrophysics* **365**, L36–L44. issn: 1432-0746. <http://dx.doi.org/10.1051/0004-6361/20000044> (Jan. 2001).
6. Córdova, F. A., Mason, K. O., Priedhorsky, W. C. & Citterio, O. The Optical Monitor on XMM. *Bulletin of the American Astronomical Society* **21**, 1137 (Sept. 1989).
7. Lumb, D. H. *et al.* The Optical Monitor on ESA's XMM Observatory. *Bulletin of the American Astronomical Society* **23**, 1349 (Sept. 1991).
8. Soria, R., Wu, K., Page, M. J. & Sakelliou, I. XMM-Newton optical monitor observations of LMC X-3. *Astronomy and Astrophysics* **365**, L273–L276. issn: 1432-0746. <http://dx.doi.org/10.1051/0004-6361/20000065> (Jan. 2001).
9. Audard, M. *et al.* The XMM-Newton Optical Monitor survey of the Taurus molecular cloud \*\*\*. *A&A* **468**, 379–390. <https://doi.org/10.1051/0004-6361/20066320> (2007).
10. Zane, S., Ramsay, G., Jimenez-Garate, M. A., Willem den Herder, J. & Hailey, C. J. XMM-Newton EPIC and Optical Monitor observations of Her X-1 over the 35-d beat period. *Monthly Notices of the Royal Astronomical Society* **350**, 506–516. issn: 0035-8711. eprint: <https://academic.oup.com/mnras/article-pdf/350/2/506/3888238/350-2-506.pdf>. <https://doi.org/10.1111/j.1365-2966.2004.07660.x> (May 2004).
11. Mukhin, A. *et al.* Wavelet-based image decomposition method for NuSTAR stray light background studies. *Journal of Astronomical Telescopes, Instruments, and Systems* **9**. issn: 2329-4124. <http://dx.doi.org/10.1117/1.JATIS.9.4.048001> (Oct. 2023).
12. Grefenstette, B. *et al.* StrayCats: A Catalog of NuSTAR Stray Light Observations. *Astrophysical Journal* **909** (Mar. 2021).
13. Desai, S., Mohr, J., Bertin, E., Kümmel, M. & Wetzstein, M. Detection and removal of artifacts in astronomical images. *Astronomy and Computing* **16**, 67–78. issn: 2213-1337. <https://www.sciencedirect.com/science/article/pii/S2213133716300233> (2016).
14. Wang, C.-Y., Bochkovskiy, A. & Liao, H.-Y. M. YOLOv7: Trainable bag-of-freebies sets new state-of-the-art for real-time object detectors 2022. arXiv: 2207.02696 [cs.CV].
15. Tu, Z. *et al.* MaxViT: Multi-axis Vision Transformer in Computer Vision – ECCV 2022: 17th European Conference, Tel Aviv, Israel, October 23–27, 2022, Proceedings, Part XXIV (Springer-Verlag, Tel Aviv, Israel, 2022), 459–479. isbn: 978-3-031-20052-6. [https://doi.org/10.1007/978-3-031-20053-3\\_27](https://doi.org/10.1007/978-3-031-20053-3_27).
16. Maaz, M. *et al.* Class-agnostic Object Detection with Multi-modal Transformer 2022. arXiv: 2111.11430 [cs.CV].
17. Zong, Z., Song, G. & Liu, Y. DETRs with Collaborative Hybrid Assignments Training 2023. arXiv: 2211.12860 [cs.CV].
18. Srivastava, S. & Sharma, G. OmniVec: Learning robust representations with cross modal sharing 2023. arXiv: 2311.05709 [cs.CV].
19. Wang, W. *et al.* Image as a Foreign Language: BEiT Pretraining for All Vision and Vision-Language Tasks 2022. arXiv: 2208.10442 [cs.CV].
20. Hümmer, C. *et al.* VLTSeg: Simple Transfer of CLIP-Based Vision-Language Representations for Domain Generalized Semantic Segmentation 2023. arXiv: 2312.02021 [cs.CV].
21. Erisen, S. SERNet-Former: Semantic Segmentation by Efficient Residual Network with Attention-Boosting Gates and Attention-Fusion Networks. <https://arxiv.org/abs/2401.15741> (2024).
22. Fang, Y. *et al.* EVA: Exploring the Limits of Masked Visual Representation Learning at Scale 2022. arXiv: 2211.07636 [cs.CV].
23. Wang, W. *et al.* InternImage: Exploring Large-Scale Vision Foundation Models with Deformable Convolutions 2023. arXiv: 2211.05778 [cs.CV].
24. Liu, Z. *et al.* Swin Transformer: Hierarchical Vision Transformer using Shifted Windows 2021. arXiv: 2103.14030 [cs.CV].
25. He, K., Gkioxari, G., Dollár, P. & Girshick, R. Mask R-CNN 2018. arXiv: 1703.06870 [cs.CV].
26. Xu, X. *et al.* An Improved Swin Transformer-Based Model for Remote Sensing Object Detection and Instance Segmentation. *Remote Sensing* **13**. issn: 2072-4292. <https://www.mdpi.com/2072-4292/13/23/4779> (2021).
27. Merz, G. *et al.* Detection, instance segmentation, and classification for astronomical surveys with deep learning (deep-disc): detectron2 implementation and demonstration with Hyper Suprime-Cam data. *Monthly Notices of the Royal Astronomical Society* **526**, 1122–1137. issn: 0035-8711. eprint: <https://academic.oup.com/mnras/article-pdf/526/1/1122/53263083/stad2785.pdf>. <https://doi.org/10.1093/mnras/stad2785> (Sept. 2023).
28. Sortino, R. *et al.* Radio astronomical images object detection and segmentation: a benchmark on deep learning methods. *Experimental Astronomy* **56**, 293–331. issn: 1572-9508. <http://dx.doi.org/10.1007/s10686-023-09893-w> (May 2023).
29. Hausen, R. & Robertson, B. Partial-Attribution Instance Segmentation for Astronomical Source Detection and Deblending 2022. arXiv: 2201.04714 [astro-ph.IM].
30. Tanoglidis, D. *et al.* DeepGhostBusters: Using Mask R-CNN to Detect and Mask Ghosting and Scattered-Light Artifacts from Optical Survey Images 2021. arXiv: 2109.08246 [astro-ph.IM].

<sup>3</sup>[https://app.roboflow.com/iulielisa/xmm\\_om-artefacts\\_512/](https://app.roboflow.com/iulielisa/xmm_om-artefacts_512/)

<sup>4</sup><https://www.zooniverse.org/projects/ori-j/ai-for-artefacts-in-sky-images>

31. Kirillov, A. *et al.* *Segment Anything* 2023. arXiv: 2304.02643 [cs.CV].
32. Centre, E. X.-N. S. O. *XMM-Newton Users Handbook* [https://xmm-tools.cosmos.esa.int/external/xmm\\_user\\_support/documentation/uhb/omfilters.html](https://xmm-tools.cosmos.esa.int/external/xmm_user_support/documentation/uhb/omfilters.html).
33. Reis, D., Kupec, J., Hong, J. & Daoudi, A. *Real-Time Flying Object Detection with YOLOv8* 2023. arXiv: 2305.09972 [cs.CV].
34. Zhang, C. *et al.* *Faster Segment Anything: Towards Lightweight SAM for Mobile Applications* 2023. arXiv: 2306.14289 [cs.CV].
35. Kuhn, H. W. The Hungarian method for the assignment problem. *Naval Research Logistics Quarterly* 2, 83–97. eprint: <https://onlinelibrary.wiley.com/doi/pdf/10.1002/nav.3800020109>. <https://onlinelibrary.wiley.com/doi/abs/10.1002/nav.3800020109> (1955).